

1 Variety of the drift pumice clasts from the 2021 Fukutoku-Oka-no-Ba eruption, Japan.
2
3 Kenta Yoshida*, Yoshihiko Tamura, Tomoki Sato, Takeshi Hanyu, Yoichi Usui, Qing Chang, Shigeaki
4 Ono
5
6 Research Institute for Marine Geodynamics, Japan Agency for Marine-Earth Science and Technology,
7 Natsushima-cho 2-15, Yokosuka, 237-0061 Japan.
8
9 Correspondence
10 Kenta Yoshida, Natsushima-cho 2-15, Yokosuka, 237-0061 Japan. E-
11 mail:yoshida_ken@jamstec.go.jp
12
13 Funding Information
14 Japan Society for the Promotion of Science, KAKENHI, Grant Nos. JP19K14825 and JP19H01999
15 to K.Y.
16 The Joint Usage and Research Program of the Earthquake Research Institute, the University of
17 Tokyo, No. ERI JURP 2021-B-01.
18 NOZOMI Farm.

19

20

21

This is a non-peer reviewed preprint that has been submitted to Island Arc; future versions may have different content.

22 Abstract

23 Pumice rafts that arrived at the Nansei Islands, Japan, provided a unique opportunity to investigate the
24 Fukutoku-Oka-no-Ba (FOB) eruption of August 2021. Despite drifting for two months for ~1300 km,
25 the drift pumice raft had a large volume and contained a variety of pumice clasts, some of which were
26 deposited during a high tide in a typhoon, while others were washed up on a sandy beach. Most of the
27 drift pumice clasts are gray in color, vesicular, and have a groundmass containing black enclaves. Rare
28 black pumice and the main gray pumice components have similar trachytic compositions, with SiO_2
29 = 61–62 mass% and total alkalis = 8.6–10 mass% (on an anhydrous basis). Both pumice types contain
30 clinopyroxene, plagioclase, and rare olivine phenocrysts. Thin-section observations show that the gray
31 pumice has more elongated vesicles as compared with the black pumice that has spherical vesicles,
32 even where the two types of pumice are in the same clast. The glass in the black pumice is transparent
33 and brown in color, while that in the gray pumice is colorless. No micro or nano-crystals were observed
34 during electron and optical microscopy. Raman spectra of the brown-colored glass exhibit a clear
35 magnetite peak, suggesting magnetite nanolites cause the brown color. High-Mg olivine in the black
36 pumice has an equilibrium temperature of 1240 °C and a rim diffusion profile indicative of re-
37 equilibration with the surrounding melt over a period of hours to days.

38 The textural relationships between the gray and black pumice suggest that the black pumice had
39 become black and viscous before the two types of pumice mixed. Therefore, crystallization of
40 magnetite nanolites and a corresponding increase in melt viscosity were important in the eruption
41 preparation process, which then resulted in a large-scale Plinian eruption.

42

43 Keywords: Fukutoku-Oka-no-Ba, Izu-Bonin-Mariana arc, Plinian eruption, drift pumice, nanolite

44

45 1. Introduction

46 Fukutoku-Oka-no-Ba (FOB) volcano is located at 24°17.1'N/141°28.9'E, ~5 km north-east to
47 Minami-Ioto Island, south of mainland Japan (Fig. 1a). Five eruptions have been recorded in 1904-05,
48 1914, 1986, 2005, and 2010 ([https://www1.kaiho.mlit.go.jp/GIJUTSUKOKUSAI/kaiikiDB/kaiyo24-](https://www1.kaiho.mlit.go.jp/GIJUTSUKOKUSAI/kaiikiDB/kaiyo24-2.htm)
49 [2.htm](https://www1.kaiho.mlit.go.jp/GIJUTSUKOKUSAI/kaiikiDB/kaiyo24-2.htm)), and discoloration of the sea surface has been occasionally observed (e.g., Furukawa, 1995).
50 Geochemical analyses and petrographical observations have been conducted on pumice erupted in
51 1904, 1914, and 1986 (Tsuya, 1937; Yoshida et al., 1987; Kato, 1988; Nakano & Kawanabe, 1992).
52 Major element composition the FOB pumices are trachyte similar to the nearby Ioto volcano, which
53 magma type is rare in the Izu-Ogasawara arc. In contrast, FOB pumices are isotopically distinct from
54 the products of the Ioto, but similar to the Hiyoshi Volcanic Complex to the south of the FOB (Sun et
55 al., 1998).

56 Detailed topography and preliminary geophysical observations of the relevant area show that there
57 exists a large volcanic complex, which has a size of 15 and 30 km for EW and NW direction,
58 respectively, and rises 2000–2200 m above the surrounding ocean floor (Fig. 1b). This complex
59 consists of Kita-Fukutoku-Tai, Kita-Fukutoku caldera, and Minami-Ioto volcanoes, from north to
60 south (Ito et al., 2011). The Kita-Fukutoku Caldera has east-west and north-south length of 10 and 16
61 km, respectively (Fig. 1b). The seismic basement of the caldera has a mortar shape, which is filled by
62 low velocity and low density materials (Onodera et al., 2003). Nishizawa et al. (2002) suggested the
63 existence of partial melts below the caldera at >1.5–2 km beneath the sea level. FOB is a central cone
64 of the Kita-Fukutoku caldera, which have ~2 km in diameter at the bottom and the height is ~200 m.
65 The summit of FOB had an oval shape elongated NE-SW, with the length of 1.5 km and 1 km,
66 respectively, and was flat at the depth of ~30 m below sea level before the eruption (Ito et al., 2011).
67 The 2021 FOB Plinian eruption occurred from 04:30 (JST) on 13 August, reported by a local fisherman,
68 to the morning of 16 August (Japan Meteorological Agency, 2021). The eruption column reached 16
69 km in height, the tropopause of the relevant area. The total volume of the erupted pumices was
70 estimated to be $100\text{--}500 \times 10^6 \text{ m}^3$ (Oikawa et al., 2021). These pumices were ejected high in the air,
71 fell on the ocean surface and started floating. A large pumice raft was observed by satellite images at
72 08:00, 3–4 h after the eruption started (Ikegami, 2021). After the eruption, two small islands were
73 observed as “()” shape, then eastern one disappeared within a month (Geospatial Information
74 Authority of Japan, 2021).

75 Pumice rafting is typically observed once a decade worldwide (e.g., Bryan et al., 2012), where silicic
76 magma erupted explosively beneath the ocean. The 1986 FOB eruption also generated pumice rafts,
77 and large amounts of drift pumice clasts arrived at numerous locations, including the Nansei Islands,
78 to where the pumice clasts were transported for ~1300 km by the Kuroshio Counter-current after a
79 duration of >4 months (Fig. 1a; Yoshida et al., 1987; Kato, 1988; Mori et al., 1992). Ocean bottom
80 observatory instruments also drift from the Izu–Bonin arc towards the Nansei Islands, which are ~
81 1700 km apart (Tada et al., 2021). Ocean current simulations indicate that the drift from the Izu–Bonin
82 arc to the Nansei Islands takes <6 months, but depends on the seasonal current and wind conditions
83 (Tada et al., 2021).

84 The 2021 FOB pumice rafts travelled westward after the eruption. The RV *Keifu-Maru* of the Japan
85 Meteorological Agency collected samples of floating pumices at 25°30.3'N/138°53.3'E on 22 August
86 2021 (Japan Meteorological Agency, 2021). Subsequently, the drift pumice rafts arrived at the Nansei
87 Islands in early October, ~2 months after the eruption. The 2021 pumice raft drifted twice as fast as
88 the 1986 FOB pumice raft, possibly due to the seasonal change of the Kuroshio Counter-current that
89 is thought to be weakened in the winter season (Uchiyama et al., 2016). We undertook comprehensive
90 analyses of the *Keifu-Maru* samples and drift pumice clasts collected from several locations on the
91 Nansei Islands. Petrographic observations revealed a variety of pumice types originated from the 2021

92 eruption. In the present paper, we describe the textural and geochemical characteristics of the collected
93 pumice clasts, and discuss the mechanisms of the 2021 FOB eruption.

94

95 2. Methods

96 Mineral compositions were determined with a field emission gun electron microprobe (EPM) analyzer
97 equipped with five wavelength-dispersive X-ray detectors (JXA-8500F; JEOL) at Japan Agency for
98 Marine-Earth Science and Technology (JAMSTEC; Yokosuka, Japan). Natural and synthetic standards
99 were used to calibrate the quantitative analyses. The analytical conditions were 15 kV and 10 nA for
100 the accelerating voltage and beam current, respectively, except for the olivine analyses. For olivine,
101 we used an accelerating voltage of 20 kV and beam current of 25 nA.

102 Raman spectra were obtained with a Raman spectrophotometer (RAMANtouch VIS-HP-MAST;
103 Nanophoton) equipped with a 532 nm semiconductor green laser at JAMSTEC. The laser power on
104 the sample surface was ~ 2 mW, and data were acquired in 2×20 s cycles. The spectrometer was
105 calibrated to the Raman peak of a Si wafer (520.7 cm^{-1}).

106 Whole-rock major element compositions of the pumice clasts were determined by X-ray fluorescence
107 (XRF) spectrometry (Rigaku ZSX Primus II) following the analytical procedure of Tani et al. (2006)
108 and sample preparation methods of Sato et al. (2020). Prior to analysis, the pumice samples were
109 crushed to pebble size (5-10 mm) and soaked in hot water (~ 40 °C) for 0–3 days. The clasts were then
110 repeatedly boiled in Milli-Q water in a microwave oven until addition of a AgNO_3 solution showed
111 that precipitation of AgCl did not occur. After desalinization, all samples were washed with Milli-Q
112 water and acetone in an ultrasonic bath, and powdered in an agate mortar or with a Multi-beads
113 Shocker pulverizer. Finally, a mixture of 0.4 g of sample powder and 4 g of $\text{Li}_2\text{B}_4\text{O}_7$ was fused and
114 made into a glass bead for XRF analysis. Accuracy and reproducibility of the major element data are
115 better than $\pm 1\%$ and $\pm 2\%$ (relative standard deviations), respectively. We also analyzed trace element
116 composition of whole-rock using solution mode ICP-MS (iCAP Qc, ThermoFisher Scientific). Rock
117 powder was digested by acids of HF, HClO_4 , and HNO_3 .

118 Trace elements of selected melt inclusions and glass in vesiculated groundmass were determined by
119 LA-ICP-MS which is a sector-field type inductively coupled plasma-mass spectrometer (Element XR,
120 ThermoFisher Scientific) combined with femto-second laser ablation (FsLA: OK-Fs2000K, OK Lab.)
121 installed at JAMSTEC (Kimura and Chang, 2012). Ablated spot is $30 \mu\text{m}$ in diameter and $\sim 20 \mu\text{m}$ in
122 depth. BCR-2G (basalt standard glass issued by the United States Geological Survey) was used as
123 external calibration standard. Any contaminations from surface and proximal phases were checked by
124 the time-resolving profiles of the signal and turned out to be negligible. During the analysis, 100%
125 normalized major element compositions are also obtained.

126 The mass-normalized susceptibility of the pumice clasts was measured with a kappabridge (KLY-4;

127 AGICO).

128

129 3. Field occurrence of the drift pumice clasts

130 Pumice clasts that had drifted to the Nansei Islands were first reported from Kita-daito Island by local
131 residents via Twitter (https://twitter.com/ufuagari_jima/status/1445317054043602945) on 5 October
132 2021. The drift pumice clasts were reported on Kikai Island on 10 October, and they continued to other
133 islands located farther west, finally the arrival were reported from Izu Islands and Boso Peninsula on
134 Mid November (Fig. 1a). The first identification of the drift pumice clasts on Kita-daito Island was on
135 5 October, because it was the first day that a ban on coastal access due to high waves caused by a
136 typhoon was lifted. An interview with the local residents suggests that the pumice raft was offshore
137 on 30 September, the day of the typhoon attack (Fig. 1a). On Minami-daito Island, a large amount of
138 drift pumice clasts was also deposited in a coastal area (i.e., Kaigunbo pool). At Kaigunbo pool, some
139 pumice clasts became trapped in crevices up to 1 m above sea level during a normal high tide (Fig.
140 2a-b). Other occurrences of pumice clasts include those collected on a rocky beach a short distance
141 from the shoreline which was not tide-related (Fig. 2c). These occurrences suggest that the pumice on
142 Minami-daito Island was washed onshore by storm waves (Goto et al., 2011) and were then protected
143 from the rising tide. The samples from Kita- and Minami-daito islands are relatively small in size (up
144 to 5-10 cm).

145 In contrast, the pumice clasts on Kikai Island and islands farther west were deposited as “moraine-
146 like” features on the shorelines of sandy beaches at high tide (Fig. 2d). At low tide, there were rocks
147 and mudflats on the seaward side of the pumice moraines, but almost no pumice. The amount of
148 pumice deposited varied greatly from beach to beach, possibly due to the orientation of the beach and
149 the direction of waves and winds on the days around when the pumice was deposited. The pumice
150 clasts deposited on the sandy beach are occasionally large (>10 cm).

151 The differences in pumice depositional patterns reflect variations in coastal topography. Given that the
152 coasts of Kita- and Minami-daito islands have steep cliffs and no sandy beaches, almost no pumice
153 was deposited these islands. Kikai Island and islands farther west generally have sandy beaches, and
154 drifting materials are easily beached (and subsequently carried away) depending on the direction of
155 the wind and tide.

156 The drift pumice clasts described below were collected from Kita- and Minami-daito islands and sandy
157 beaches of Kikai Island, Amami Oshima, and Okinawa Island (Fig. 1a).

158

159 4. Pumice classification

160 The pumice clasts collected from the drifting pumice raft by the RV *Keifu-Maru* (samples 15, 18, and

161 19 provided by the JMA, herein referred to as FOB-JMA-15, -18, and -19, respectively) have similar
162 characteristics to the drift pumice clasts collected from the Nansei Islands. Notably, the large FOB-
163 JMA-18 sample has a highly vesiculated interior (Fig. 3a-b), whereas such highly vesiculated pumice
164 was rarely observed in the drift pumice clasts collected from the Nansei Islands. Regardless of the
165 deposited locations, the characteristics of drift pumice clasts are similar and they can be classified into
166 six types, based on color and texture: gray, black, brown, pale gray, amber, and streaky (Fig. 3c). The
167 details of each type are described below.

168 **Gray type:** This is the most abundant pumice type (>90%). The drift pumice clasts collected by the
169 RV *Keifu-Maru* (samples FOB-JMA-15, 18, and 19) are also classified as this type. The pumice
170 consists mainly of gray-colored vesicular glass, containing dark-colored fragments (Fig. 3a and c) that
171 are termed as black xenoliths (Kato, 1988) or mafic inclusions (Sun et al., 1998), whose appearance
172 is sometimes compared to “chocolate-chip cookie.” The fragments are a few millimeters to 1 cm in
173 size. Hereafter, we refer to these as black enclaves. The vesicles in the groundmass are occasionally
174 elongate.

175 **Black type:** This type occurs as either independent black pumice clasts or sub-clasts within the gray
176 pumice (Fig. 3c). The independent black pumice clasts are not common, and the sub-clasts in the gray
177 pumice are more common. Most black pumice clasts do not contain elongate vesicles or evidence for
178 ductile deformation.

179 **Brown type:** This pumice type occurs occasionally as a transitional form of the gray pumice. The
180 brown pumice bands are parallel to the elongate groundmass texture.

181 **Pale gray type:** The pale gray pumice has a groundmass that is a much darker gray color as compared
182 with the gray type. This type is transitional with the gray pumice.

183 **Amber type:** The amber type pumice has an amber-colored vesicular groundmass that contains coarse
184 bubbles (up to several millimeters) and is harder than the other types of pumice.

185 **Streaky type:** This type of pumice consists of banded gray and black pumice. The bands of black
186 pumice (up to 5 mm wide) are generally thinner than those of the gray pumice.

187 In addition to the above six pumice types, some pumice clasts have blocky and glassy surfaces that
188 possibly formed by quenching.

189

190 5. Petrography and Geochemistry

191 5.1 Petrography and mineral chemistry

192 The pumice clasts consist mainly of clinopyroxene (Cpx), plagioclase (Pl), rare olivine (Ol), and a
193 groundmass of vesiculated glass and minor amounts of apatite and opaque minerals (Fig. 4a).
194 Representative mineral and glass analyses are listed in Tables 1–3, and whole-rock compositions
195 determined by XRF spectrometry are listed in Table 4.

196 Two generations of Ol, Cpx, and Pl were recognized based on optical and electron microscopic
197 observations.

198 Olivine occurs in two populations. One is phenocrysts or inclusions in Pl phenocrysts in the
199 vesiculated groundmass of the gray pumice, with Mg# values ($\text{Mg}/[\text{Mg}+\text{Fe}] \times 100$) of ~65 and almost
200 free of NiO. The other type occurs as euhedral phenocrysts in the vesiculated groundmass of black,
201 and has Mg# = 92 (Fig. 4c and g), NiO (up to 0.17 mass%), and Al_2O_3 (~0.019 mass%). This high-Mg
202 Ol has a low-Mg rim with Mg# = ~80 and, towards the rim, a clear diffusion profile is ~20 μm thick
203 (Fig. 4g). High-Mg Ol also occurs in the pale gray pumice, with lower Mg# values of up to 87. A few
204 Ol micro-crystals were observed in the glassy groundmass of the black pumice, which are up to ~5
205 μm in diameter and have a similar composition as the low-Mg Ol (Mg# = ~65).

206 Clinopyroxene occurs as phenocrysts in all pumice types. The Cpx has a diopside (Di) to augite (Aug)
207 composition (Fig. 4e), with Di cores with higher Mg# values (~95) and Aug rims with lower Mg#
208 values (~75). Cpx also occurs as micro-crystals in the glassy groundmass of the black and gray pumice,
209 and is Aug with Mg# values of ~75.

210 Plagioclase occurs as phenocrysts (up to 5 mm in size) in the groundmass of gray pumice, and is
211 andesine with Ca-rich cores (An_{45}) and Na-rich rims (An_{33}) (Fig. 4d). Pl in the black pumice is fine-
212 grained (<300 μm) and homogeneous, with An_{40-45} . Some Pl that occurs as white-colored enclaves
213 and micro-crystals in the black enclaves has an anorthite composition with An_{89-95} . Rare amphibole
214 coexists with the anorthitic plagioclase (Fig. 4f), and dendritic crystals within melt inclusions in high-
215 Mg Ol.

216 The opaque minerals are generally Ti-bearing magnetite (Mag), while those occurring as inclusions in
217 Pl and Cpx are rarely Fe-sulfide. High-Mg type Ol occasionally contained chromian spinel (Cr-Spl).
218 Plagioclase occasionally contains abundant brown-colored melt inclusions (Fig. 4a). Melt inclusions
219 in low-Mg Ol are brown-colored, while those in high-Mg Ol are colorless (Fig. 4b).

220 Black enclaves have two types of occurrences, called type-1 and type-2. Type-1 black enclaves have
221 a dense and fine-grained groundmass consisting mainly of Pl, Cpx, and intergranular glass with
222 phenocrysts of Cpx and Ol (Fig. 5a). Type-2 black enclave have an equigranular texture and consist
223 of Cpx, Ol, and Pl, with minor amounts of magnetite and intergranular glass (Fig. 5b). Ol phenocrysts
224 in type-1 black enclaves are high-Mg and have NiO contents up to 0.12 mass%. Cpx phenocryst in
225 type-1 black enclaves is diopside composition with Mg# values of 92–95 that decrease to 83 in the
226 rims. Pl occurs as fine-grained crystals in the groundmass of type-1 black enclaves, and has high
227 anorthite contents of up to An_{87} . In contrast, type-2 black enclaves contain Cpx, Ol, and Pl that have
228 similar compositions as those in the vesicular groundmass of the gray pumice, except for the cores of
229 zoned Pl. Pl in type-2 black enclaves exhibited decrease in anorthite content from core (An_{82}) to rim
230 (An_{32}) (Fig. 5d and e).

231

232 5.2 Glass and whole-rock geochemical compositions

233 The texture of vesicles vary in the different types of pumice. Gray pumice comprises colorless glass
234 with the elongate vesicles, whereas black pumice has a relatively undeformed vesicle texture and
235 brown-colored glass (Fig. 6a–c). Amber pumice has a completely different texture, comprising large
236 bubbles and relatively high glass connectivity (Fig. 6d), resulting in its relatively high hardness.

237 Vesicular glass in the groundmass is transparent and brown in the black and brown pumices, whereas
238 that in the gray pumice is colorless (Fig. 6a–b). Glass in the pale gray pumice is also colorless, but
239 contains abundant micro-crystals (nanolites) visible under microscope, which are either rectangular or
240 circular in shape (Fig. e–f). These black nanolites were identified as magnetite by Raman microscopy
241 (Fig. 6g). Brown-colored glass in the pale gray pumice only occurs around or inclusions in phenocrysts.
242 Textural characteristics also vary amongst the different types of pumice. Figure 6c shows a scanning
243 electron microscopy (SEM) image of the contact between black and gray pumice. The gray pumice
244 domain contains highly elongate vesicles as compared with the adjacent black pumice that has a bubble
245 aspect ratio of ~1.

246 Differences in the brown-colored and colorless glass were further investigated by Raman spectroscopy.
247 The Raman spectrum of the brown-colored glass shows a clear peak at 663 cm^{-1} that is attributed to
248 magnetite (Fig. 6g), even though no micro-crystals were visible under the microscope. In contrast, the
249 663 cm^{-1} peak did not appear in the spectra of the colorless glass in gray and pale gray pumices.

250 The glass compositions determined by EMP analyses exhibit trachytic compositions, regardless of the
251 pumice type (Fig. 7a). In particular, the black and gray pumices have very similar compositions, while
252 the amber pumice is relatively enriched in CaO, MgO, and total FeO (Fig. 7b).

253 Intragranular melt in type-1 black enclaves has lower SiO_2 contents as compared with the vesiculated
254 glass, whereas intragranular melt in type-2 black enclaves has similar compositions to vesiculated
255 glass.

256 Melt inclusions in Pl, augitic Cpx, and low-Mg Ol have similar compositions as the groundmass glass,
257 whereas those in diopsidic Cpx and high-Mg Ol have low SiO_2 contents ($\text{SiO}_2 = 50\text{--}55\text{ mass\%}$) and
258 are basaltic to basaltic-andesitic in composition (Fig. 7a). Basaltic melt inclusions occasionally contain
259 dendritic minerals, which are difficult to analyze. The most SiO_2 -rich melt inclusion was discovered
260 in a Aug-Cpx enclosed in Pl (Fig. 4a), and had a rhyolitic composition with $\text{SiO}_2 = 68\text{--}69\text{ mass\%}$ (Fig.
261 7a).

262 Whole-rock compositions of the gray, black, and amber pumice clasts were determined by XRF
263 spectrometry, and all had trachytic compositions regardless of pumice type (Fig. 7a). Pale gray and
264 brown pumice grade into gray pumice, and we did not undertake separate whole-rock analyses of these
265 types.

266 Selected mafic melt inclusions in type-1 back enclaves and vesicular (trachytic) glass of gray pumice
267 are analyzed and shown in spider diagram (Fig. 7c). Groundmass of type-1 black enclave was also

268 measured as the mixture of intergrain melt and groundmass minerals. Figure 7c also shows whole-
269 rock trace element compositions of gray pumice (FOB-JMA-15, 18, 19). The whole-rock composition
270 and the trachytic glass of gray pumice showed similar trace element patterns to that of the 1986
271 eruption. In contrast, mafic melt inclusions exhibited different patterns such as positive anomaly of Sr,
272 negative anomaly of Pr, Zr, and Hf. Although measured as mixtures, groundmass of type-1 BI
273 exhibited intermediate compositions between trachytic glass and mafic inclusions.
274 Mass-normalized magnetic susceptibility was determined on the black and gray pumices (Table 5).
275 The black pumice had a higher magnetic susceptibility than the gray pumice.
276

277 6. P - T calculation

278 Table 6 summarizes the coexisting mineral and melt assemblages observed in the drift pumice clasts.
279 At least two generations can be clearly identified: (1) those associated with mafic melt, including high-
280 Mg Ol and diopsidic Cpx; and (2) those associated with trachytic melt, including low-Mg Ol, augitic
281 Cpx, Mag, and Pl (An₄₄₋₃₃).

282 Given that the high-Mg Ol in the black pumice contains Cr-Spl, we applied the Al-in-Ol thermometer
283 (Coogan, 2014). The compositional pair of an Ol core (Mg# = 92) and Cr-Spl of the black pumice
284 (KGB-1) yielded a temperature of 1242 °C.

285 Growth conditions of the augitic Cpx were estimated using the magnetite geothermometer (Canil and
286 Lacourse, 2020) for Mag inclusions in Cpx (Fig. 4e) and the Cpx single mineral geobarometer (Petrelli
287 et al., 2020) for associated Cpx. Mag in augitic Cpx (FSD-1) yielded ~930°C while pressures for
288 associated Cpx is ~250 MPa.

289 The Cpx single mineral geobarometer applied to Cpx containing a rhyolitic melt inclusion (Fig. 4a)
290 yielded a pressure of 409 MPa, which is slightly higher than that obtained from the augitic Cpx
291 containing trachytic melts.

292

293 7. Discussion

294 7.1 Different color types of the drift pumice clasts

295 Despite the different colors of the pumice clasts, whole-rock compositions of the 2021 FOB pumice
296 are similar. The drift pumice clasts from the 1986 eruption also included gray and black (described as
297 dark-gray in the literature) pumice with similar whole-rock compositions including the Fe₂O₃/FeO
298 ratio (Kato, 1988). Raman spectroscopy revealed that the brown-colored glass contained magnetite,
299 although no micro-crystals were observed under the microscope (Fig. 6g). Such a Raman signature is
300 known to originate from sub-microscopic magnetite nanoparticles (Di Genova et al., 2017; Lerner et
301 al., 2021). Based on transmitted electron microscope (TEM) observations of volcanic glass that

302 revealed a crystal size gap of crystalline nanoparticles between <30 nm and >1 μm, Mujin et al. (2017)
303 defined the term “ultrananolite” for grains smaller than <30 nm and the term “nanolite” for a grain
304 size of 30–1000 nm. We did not perform TEM observations and only detected Mag nanoparticles based
305 on Raman spectroscopy. As such, we here use the term nanolite to describe the sub-microscopic Mag
306 in our glass samples. The precipitation of Mag nanolites is consistent with the higher magnetic
307 susceptibility of the black pumice as compared with the gray pumice.

308 Paulick and Franz (1997) documented very similar characteristics for trachytic pumice in the Meidob
309 volcanic field, Sudan. They measured the Fe₂O₃/FeO ratios and magnetic susceptibility for the pumice
310 erupted at 5 ka, which revealed a weak positive correlation between whole-rock Fe₂O₃ contents and
311 magnetic susceptibility. In their study, glass in dark gray pumice was also transparent and brown, and
312 they concluded that the brown color was caused by sub-microscopic Mag precipitation in the glass.
313 Schlinger et al. (1986, 1988) identified nano-crystals of Fe oxides in volcanic glasses by TEM
314 observations. In samples from southern Nevada, the size of the Fe oxide grains was up to 140 nm for
315 a quenched sample, and greater in the sample that was more slowly cooled (up to 800 nm; Schlinger
316 et al., 1988). Schlinger et al. (1986) performed heating experiments on colorless, precipitate-free, glass
317 shards at 950°C for 5 min, which resulted in darkening of the glass and precipitates forming on the
318 scale of TEM analysis.

319 A recent experimental study by Di Genova et al. (2020) revealed that nanolite precipitation is a
320 transient phenomenon that is preserved at a high cooling rate of 10–20°C/s, whereas slow cooling
321 allowed microlites to form. Di Genova et al. (2020) suggested that a small amount (~ 4 vol.%) of
322 nanoparticles and a shear rate of 3.5 s⁻¹ would increase the viscosity by a factor of 10² within 100 s of
323 nanolite formation. Given that the brown-colored glass of the present study contains nanolites and that
324 this increased its viscosity, this can explain the less deformed texture of the black pumice as compared
325 with the gray pumice (Fig. 6c).

326

327 7.2 Timescales of magma mixing

328 High-Mg Ol found in type-1 black enclaves and black pumice indicated that the mafic magma injection
329 involved in the 2021 FOB explosive eruption. Black pumice clasts are the evidence of heating by the
330 mafic magma of >1200°C and the clear diffusion profile at the rim recorded the timescales of the
331 magma mixing.

332 To assess the timescales of the mafic magma injection, diffusion modeling of Fe–Mg zoning in Ol was
333 undertaken following the methods of Costa and Dungan (2005) and Viccaro et al. (2016). Diffusion
334 coefficients for Fe–Mg in Ol along *c*-axis were calculated following Costa and Chakraborty (2004):

$$335 \quad D_c^{\text{Fe-Mg}} = 5380 \times \left(\frac{f_{\text{O}_2}}{10^{-12}} \right)^{1/6} \times 10^3 \left(\frac{86 - F_{\text{O}}}{100} \right) \exp\left(\frac{-226000}{8.314 \times T(\text{K})} \right) \quad (1)$$

336 where the diffusion coefficients for the other axis are assumed to be:

337
$$D_c^{\text{Fe-Mg}} \sim 6D_a^{\text{Fe-Mg}} \sim 6D_b^{\text{Fe-Mg}} \quad (2)$$

338 Therefore, the pressure dependence of the diffusion coefficients was ignored. The following form of
339 Fick's second law (in one dimension) with concentration-dependent diffusion coefficients was used
340 for the diffusion modelling:

341
$$\frac{\partial c}{\partial t} = \frac{\partial}{\partial x} \left(D \frac{\partial c}{\partial x} \right) \quad (3)$$

342 Given that the high-Mg Ol had a plateau core composition of Mg# = 92 (Fig. 4g), we used this as the
343 initial value. The rim composition of Mg# = 81 (point A in Fig. 4b) was regarded as the boundary
344 condition at the rim for the calculation (i.e., we used a time-invariant constant composition at the rim).
345 Given that the diffusion rim is very narrow, point B yielded a higher Mg# due to a small mis location
346 of the analytical site. We fitted between point A and corresponding side.

347 In the present study, the crystal orientation was not determined, and thus diffusional anisotropy was
348 not strictly evaluated. The diffusion modeling was performed assuming a direction parallel to the *c*-
349 axis and the calculated time could be up to 36 times larger than that determined. Diffusion coefficients
350 were calculated at T = 1242°C (derived from Ol–Cr–Spl thermometry) and f_{O_2} values varying from
351 QFM+1 to +3 following the calibration of Myers and Eugster (1983), although 1242 °C is slightly out
352 of the calibration range.

353 Figure 4g shows the best-fit model and Figure 7d shows the relationship between the calculated time
354 and f_{O_2} values. Assuming that diffusion occurred parallel to the *c*-axis, the calculated time varies from
355 11 to 24 hours for the f_{O_2} range from QFM+1 to +3. Depending on the crystal orientation, the estimated
356 time becomes as long as 50 d.

357

358 7.3 Variable pumice types and their role during the explosive eruption

359 Based on textural and geochemical characteristics, different types of pumice had different roles in the
360 explosive eruption of FOB in 2021. Mitchell et al. (2021) suggested that the pumice clasts form a
361 floating raft and those that suddenly sink to the seafloor have distinct micro-textures (i.e., the floating
362 pumice has a higher vesicle number density and lower pore space connectivity). This could bias the
363 pumice clasts that were sampled. However, the range of drift pumice clasts sampled does partly
364 represent the nature of the 2021 FOB eruption.

365 The main gray pumice represents the magma reservoir of the FOB. The texture of type-2 black
366 enclaves suggests an origin from a highly crystalized part of the magma reservoir, such as crystal mush.
367 In contrast, type-1 black enclaves and high-Mg olivine in black and pale gray pumice record mafic
368 magma involvement. As groundmass of type-1 black enclaves shows intermediate composition
369 between trachytic and mafic melts (Fig. 7c), type-1 black enclaves represent the mixing nature of the
370 ascending mafic magma and trachytic magma reservoir (Fig. 8). Mafic melt inclusions in both
371 diopsidic Cpx and high-Mg Ol indicate that mafic magma triggered the eruption. Explosive eruption

372 of silicic magma can be triggered by the cryptic mafic magma injection (e.g., Tamura et al., 2003;
373 Shukuno et al., 2006; Tamura et al., 2009). Such involvement are sometimes recognized as co-
374 occurrence of bimodal mafic and silicic clastic materials, although drift pumice clasts in this study all
375 yielded trachytic compositions.

376 In the present case, black pumice could have been heated by injected mafic magma; however, the
377 whole-rock composition does not change and the high-Mg Ol and Di-Cpx phenocrysts (should be
378 called as xenocrysts) only recorded it. Transport process of xenocrysts from the mafic magma to
379 trachytic magma without changing whole-rock compositions remains unclear. When hydrous mafic
380 magma injected into resident felsic crystal-rich mushes, mafic magma dramatically crystallizes due to
381 the water escape into the felsic magma and corresponding change in liquidus temperature (Pistone et
382 al., 2017). The solidification of hot mafic magma essentially releases the latent heat that can enhance
383 the rejuvenation of the crystal mush. Injected mafic magma would either (1) get highly solidified and
384 could not ejected by the eruption, or (2) sink suddenly around the FOB and we cannot obtain such
385 samples from the drift pumice raft.

386 Despite the similar whole-rock geochemical compositions of the gray and black pumice, we rarely
387 observed a gradual transition between them. Adjacent gray and black pumice generally have clear
388 boundaries and distinct textures (Fig. 6c), indicating the black pumice magma was highly viscous prior
389 to mingling and that the eruption occurred soon after mingling. The diffusion modeling of Ol also
390 showed a short timescale of black pumice activity, from hours to days (Fig. 7d). Fe oxide nanolites are
391 considered to form due to cooling and/or diffusive H₂O loss (Danyushevsky et al., 2002; Di Genova
392 et al., 2017, 2018), also indicating short timescales. The presence of magmatic nanolites can enhance
393 heterogeneous bubble nucleation and lead to an explosive eruption of silicic magma (Ceseres et al.,
394 2020).

395 Although the detailed mechanisms of the 2021 FOB Plinian eruption remain unclear, the common and
396 co-occurrence of the nanolite-bearing black pumice within gray pumice might record an important
397 process involved in the explosive eruption. To sum up, ascending mafic magma evidenced by the melt
398 inclusions in high-Mg Ol and diopsidic Cpx heated certain amount of trachytic magma reservoir under
399 FOB, triggering the 2021 explosive eruption (Fig. 8). More detailed micro-textural observations of the
400 mingled black and gray pumice clasts and/or streaky pumice might provide further insights into the
401 magmatic systems of the FOB and neighboring volcanoes in the Mariana arc.

402

403 Supplementary Materials

404 Trace element analysis data of vesiculated glass, mafic melt inclusions, and whole-rock are available
405 from the online depository materials.

406

407 Acknowledgements

408 The authors are grateful to S. Hadana of the Kitadaito Island Development Support Organization and
409 T. Komagoe of the Kikai Institute for Coral Reef Science for their help with the field survey and
410 providing pumice samples. We also thank Y. Maruya of the National Outfitters Training School
411 Okinawa Branch (NPO) for discussions about the field observations at Okinawa Island. The many
412 twitter account holders that posted about the FOB pumice are also thanked. This research was partly
413 supported by the JSPS KAKENHI (grant nos. JP19K14825 and JP19H01999 to K.Y.), the Joint Usage
414 and Research Program of the Earthquake Research Institute, the University of Tokyo (ERI JURP 2021-
415 B-01), and NOZOMI Farm.

416

417 References

- 418 Bryan, S.E., Cook, A.G., Evans, J.P., Hebden, K., Hurrey, L., Colls, P., Jell, J.S., Weatherly, D., and
419 Firm, J. (2012) Rapid, long-distance dispersal by pumice rafting. (2012) *Plos one*, 7, e40583.
- 420 Canil, D. & Lacourse, T. (2020) Geothermometry using minor and trace elements in igneous and
421 hydrothermal magnetite. *Chemical Geology*, 541, 119576.
- 422 Ceseres, F., Wadsworth, F.B., Scheu, B., Colombier, M., Madonna, C., Cimorelli, C., Hess, K.-U.,
423 Kaliwoda, M., Ruthensteiner, B., & Dingwell, D.B. (2020) Can nanolites enhance eruption
424 explosivity? *Geology*, 48, 997-1001.
- 425 Coogan, L.A., Saunders, A.D., & Wilson, R.N. Aluminum-in-olivine thermometry of primitive
426 basalts: Evidence of an anomalously hot mantle source for large igneous provinces. *Chemical*
427 *Geology*, 368, 1-10.
- 428 Costa, F. & Chakraborty, S. (2004) Decadal time gaps between mafic intrusion and silicic eruption
429 obtained from chemical zoning patterns in olivine: *Earth and Planetary Science Letters*, 227, 517–
430 530.
- 431 Costa, F. & Dungan, M. (2005) Short time scales of magmatic assimilation from diffusion modeling
432 of multiple elements in olivine. *Geology*, 33, 837-840.
- 433 Danyushevsky, L.V., McNeill, A.W., and Sobolev, A.V. (2002) Experimental and petrological studies
434 of melt inclusions in phenocrysts from mantle-derived magmas: An overview of techniques,
435 advantages and complications. *Chemical Geology*, 183, 5-24.
- 436 Di Genova, D., Sicola, S., Romano, C., Vona, A., Fanara, S., and Spina, L. (2017) Effect of iron and
437 nanolites on Raman spectra of volcanic glasses: A reassessment of existing strategies to estimate
438 the water content. *Chemical Geology*, 475, 76-86.
- 439 Di Genova, D., Caracciolo, A., and Kolzenburg, S. (2018) Measuring the degree of “nanolilization”
440 of volcanic glasses: Understanding syn-eruptive processes recorded in melt inclusions. *Lithos*,

441 318, 209-218.

442 Di Genova, D., Brooker, R.A., Mader, H.M., Drewitt, J.W.E., Longo, A., Deubener, J., Neuville D.R.,
443 Fanara, S., Shebanova, O., Anzellini, S., Arzilli, F., Bamber, E.C., Hennem, L., La Spina, G.,
444 Miyajima, N. (2020) In situ observation of nanolite growth in volcanic melt: A driving force for
445 explosive eruptions. *Science Advances*, 6, eabb0413.

446 Furukawa, H. (1995) Annual report of world volcanic eruptions in 1992, Fukutoku-oka-no-ba. *Bulletin*
447 *of Volcanology*, 57, 81-82.

448 Geospatial Information Authority of Japan (2021)
449 <https://www.gsi.go.jp/uchusokuchi/20210820fukutokuokanoba.html>

450 Goto, K., Miyagi, K., Kawana, T., Takahashi, J., & Imamura, F. (2011) Emplacement and movement
451 of boulders by known storm waves – Field evidence from the Okinawa Islands, Japan. *Marine*
452 *Geology*, 283, 66-78.

453 Ikegami, F. (2021) Pumice raft dispersion of Fukutoku-oka-no-ba 2021 eruption. The abstract volume
454 of the annual meeting of the Volcanological Society of Japan, A2-02.

455 Ito, K., Kato, S., Takahashi, M., Saito, A. (2011) Volcanic topography of Fukutoku-Oka-no-ba volcano
456 in Izu-Ogasawara arc after 2010 eruption. *Report of Hydrographic and Oceanographic*
457 *Researches*, 47, 9-13.

458 Japan Meteoric Agency (2021) Monthly volcanic activity reports of Fukutoku-oka-no-ba, 2021 August.
459 [https://www.data.jma.go.jp/svd/vois/data/tokyo/STOCK/monthly_v-](https://www.data.jma.go.jp/svd/vois/data/tokyo/STOCK/monthly_v-act_doc/tokyo/21m08/331_21m08.pdf)
460 [act_doc/tokyo/21m08/331_21m08.pdf](https://www.data.jma.go.jp/svd/vois/data/tokyo/STOCK/monthly_v-act_doc/tokyo/21m08/331_21m08.pdf) (Webpage title was translated by the authors)

461 Kato, Y. (1988) Gray pumice drifted from Fukutoku-oka-no-ba to Ryukyu Islands. *Bulletin of the*
462 *Volcanological Society of Japan Series 2*, 33, 21-30 (in Japanese).

463 Kimura, J.-I. & Chang, Q. (2012) Origin of suppressed matrix effect for improved analytical
464 performance in determination of major and trace elements in anhydrous silicate samples using
465 200 nm femtosecond laser ablation sector-field inductively coupled plasma mass spectrometry.
466 *Journal of Analytical Atomic Spectrometry*, 27, 1549-1559.

467 Mitchell, S.J., Fauria, K., Houghton, B.F., & Carey, R.J. (2021) Sink or float; microtextural controls
468 on the fate of pumice deposition during the 2012 submarine Harve eruption. *Bulletin of*
469 *Volcanology*, 83, 80.

470 Mori, S., Yamashita, H., & Goto, M. (1992) Drifted pumices from Ogasawara Arc to the coast of
471 Sagami Bay. *Bulletin of the Hiratsuka City Museum*, 15, 1-14.

472 Mujin, M., Nakamura, M., and Miyake, A. (2017) Eruption style and crystal size distributions:
473 Crystallization of groundmass nanolites in the 2011 Shinmoedake eruption. *American*
474 *Mineralogist*, 102, 2367-2380.

475 Myers, J. & Eugster, H.P. (1983) The system Fe-Si-O: Oxygen buffer calibrations to 1,500 K.
476 *Contributions to Mineralogy and Petrology*, 82, 75-90.

- 477 Nakano, S. & Kawanabe, Y. (1992) Pumices drifted to Iriomote Island in 1991. *Bulletin of the*
478 *Volcanological Society of Japan*, 37, 95-98 (in Japanese).
- 479 Nishizawa, A., Ono, T., Sakamoto, H., Matsumoto, Y., Otani, Y. (2002) Ocean bottom seismographic
480 observation at Fukutoku-okanoba submarine volcano. *Report of Hydrographic Researches*, 38,
481 101-123.
- 482 Oikawa, T., Yanagisawa, H., Ikegami, F., Ishizuka, O., Mizuochi, H., Tomiya, A., Morita, M., Nakano,
483 S., Kawaguchi, R., & Nakamura, M. (2021) The August 2021 Fukutoku Okanoba Eruption in
484 Ogasawara Islands, Japan. The abstract volume of the annual meeting of the Volcanological
485 Society of Japan, P1-34.
- 486 Onodera, K., Kato, T., Seo, N. (2003) Crustal structure in the vicinities of Fukutoku-okanoba
487 submarine volcano estimated from gravity and magnetic anomalies. *Report of Hydrographic and*
488 *Oceanographic Researches*, 39, 23-31.
- 489 Paulick, H. & Franz, G. (1997) The color of pumice: case study on a trachytic fall deposit, Meidob
490 volcanic field, Sudan. *Bulltine of Volcanology*, 59, 171-185.
- 491 Petrelli, M., Caricchi, L., & Perugini, D. (2020) Machine learning thermo-barometry: Application to
492 clinopyroxene-bearing magmas. *Journal of Geophysical Research: Solid Earth*, 125,
493 e2020JB020130.
- 494 Pistone, M., Blundy, J., Brooker, R.A., & EIMF (2017) Water transfer during magma mixing events:
495 Insights into crystal mush rejuvenation and melt extraction process. *American Mineralogist*, 102,
496 766-776.
- 497 Sato, T., Miyazaki, T., Tamura, Y., Gill, J.B., Jutzeler, M., Senda, R., & Kimura, J.-I. The earliest stage
498 of Izu rear-arc volcanism revealed by drilling at Site U1437, International Ocean Discovery
499 Program Expedition 350. *Island Arc*, 2020, e12340
- 500 Schlinger, C.M., Smith, R.M., Veblen, D.R. (1986) Geologic origin of magnetic volcanic glasses in
501 the KBS tuff. *Geology*, 14, 959-962.
- 502 Schlinger, C.M., Rosenbaum, J.G., Veblen, D.R. (1988) Fe-oxide microcrystals in welded tuff from
503 southern Nevada: Origin of remanence carriers by precipitation in volcanic glass. *Geology*, 16,
504 556-559.
- 505 Shukuno, H., Tamura, Y., Tani, K., Chang, Q., Suzuki, T. & Fiske, R. S. (2006). Origin of silicic magmas
506 and the compositional gap at Sumisu submarine caldera, Izu-Bonin arc, Japan. *Journal of Volcanology*
507 *and Geothermal Research*, 156, 187-216.
- 508 Sun, C.-H. Stern, R., Yoshida, T., & Kimura, J.-I. (1998) Fukutoku-oka-no-ba Volcano: A new
509 perspective on the Alkalic Volcano Province in the Izu-Bonin-Mariana arc. *The Island Arc*, 7,
510 432-442.
- 511 Sun, W. & McDonough, W.F. (1989) Chemical and isotopic systematics of oceanic basalts:
512 Implications for mantle composition and processes. *Geological Society London Special*

513 Publications, 42, 313-345.

514 Tada, N., Nishikawa, H., Ichihara, H., Watanabe Kayama, H., Kuwatani, T. (2021) Ocean Bottom
515 Electromagnetometer Carried From Bonin to Ryukyu Islands by Sea Currents.
516 doi:10.21203/rs.3.rs-966838/v1

517 Tamura, Y., Yuhara, M., Ishii, T., Irino, N. & Shukuno, H. (2003). Andesites and dacites from Daisen
518 volcano, Japan: partial-to-total remelting of an andesite magma body. *Journal of Petrology*, 44, 2243-
519 2260.

520 Tamura, Y., Gill, J. B., Tollstrup, D., Kawabata, H., Shukuno, H., Chang, Q., Miyazaki, T., Takahashi, T.,
521 Hirahara, Y., Kodaira, S., Ishizuka, O., Suzuki, T., Kido, Y., Fiske, R. S. & Tatsumi, Y. (2009). Silicic
522 magmas in the Izu-Bonin oceanic arc and implications for crustal evolution. *Journal of Petrology*, 50,
523 685-723.

524 Tani, K., Kawabata, H., Chang, Q., Sato, K., & Tatsumi, Y. (2006) Quantitative analyses of silicate
525 rock major and trace elements by X-ray fluorescence spectrometer: Evaluation of analytical
526 precision and sample preparation. *Frontier Research on Earth Evolution*, 2, 1-8.

527 Tsuya, H. (1937) On the volcanics of the Huzi Volcanic zone, with special reference to the geology
528 and petrology of the Idu and Southern Islands. *Bulletin of Earthquake Research Institute*, 15, 215-
529 357.

530 Uchiyama, Y., Odani, S., Yamanishi, T., Kamidaira, Y., & Mitarai, S. (2016) Impact of mesoscale
531 recirculation of the Kuroshio on asymmetric oceanic structure around Okinawa Island. *Journal*
532 *of Japan Society of Civil Engineers, Ser. B2 (Coastal Engineering)*, 72, I_481-I_486.

533 Viccaro, M., Giuffrida, M., Nicotra, E., & Cristofolini, R. (2016) Timescales of magma storage and
534 migration recorded by olivine crystals in basalts of the March-April 2010 eruption at
535 Eyjafjallajökull volcano, Iceland. *American Mineralogist*, 101, 222-230.

536 Yoshida, T., Fujiwara, S., & Aoki, K. (1987) Geochemistry of Fukutoku-oka-no-ba submarine volcano,
537 Izu-Ogasawara arc. *Research Report of Laboratory of Nuclear Science, Tohoku University*, 20,
538 202-215 (in Japanese).

539

540 Figure Caption

541

542 Figure 1.

543 (a) Index map of the Fukutoku-Oka-no-Ba (FOB) located near the Ioto Island, south of mainland Japan.
544 Summary of the arrival reports of drift pumice are shown. The track of the pumice raft originated from
545 1986's eruption is also shown. Arrival date are based on Twitter posts for 2021 eruption summarized
546 in <https://togetter.com/li/1762225>, while those of 1986 eruption are taken from Yoshida et al. (1987),
547 Kato (1988), and Mori et al. (1992). Specific events arranged in chronological order is also
548 summarized. The course of typhoon 16 passed along Japanese Islands on the end of September and
549 should have affected on pumice drifting is also shown (sourced from Japan Meteorological Agency
550 database, https://www.data.jma.go.jp/yoho/typhoon/route_map/bstv2021.html). (b) Topographic map
551 around FOB after Ito et al. (2011).

552

553 Figure 2.

554 Field occurrence of the unloaded drift pumice. (a) Kaigunbo artificial pool at the Minami-daito Island.
555 Small drift pumice clasts were observed on the rugged rock on the road, up to approximately 1m height.
556 Pumice clasts on the road were almost removed. (b) Closed view of the orange rectangle of (a),
557 showing remained pumice clasts in the rock crevices. (c) Rocky beach near the Kaigunbo pool. Large
558 number of pumice clasts were collected in the topographic low. The pumice-pooled area was isolated
559 from the sea by a wall-like topographic high of the coastal rocks. (d) Drift pumice clasts unloaded on
560 the sandy beach of the Amami-Oshima Island. Pumice clasts comprised a "pumice moraine" at the
561 high tide shoreline, while clasts did not remain at more seaward rocky area.

562

563 Figure 3

564 Photo of the typical drift pumice clasts. (a) The large sample collected by JMA RV *Keifu-Maru* (FOB-
565 JMA-18). Compared with the drift sample from the Nansei Islands, rugged surface was preserved. (b)
566 Inside of FOB-JMA-18. Central part is highly vesicular compared to the outer part. (c) Variety of
567 pumice clasts collected from the Nansei Islands. Details are described in the text.

568

569 Figure 4.

570 Photomicrograph and SEM images of the phenocryst minerals in the studied pumice. (a) Cpx and
571 brown-colored melt in Pl phenocryst in brown pumice. Brown-colored melt also surrounded the Pl
572 grain. (b) Colorless mafic melt inclusion in high-Mg Ol occurred in pale-gray pumice. Ol was
573 surrounded by trachytic melt. (c) Euhedral high-Mg Ol occurred in black pumice. Outer-most part
574 show decrease in Mg#. Cr-Spl is included. A-B line indicates the line-profile measurement shown in

575 Figure 4g. (d) Pl + Cpx phenocryst clot occurred in gray pumice. Pl exhibited An₄₄ core and An₃₅
576 rim. (e) Cpx phenocryst showing a clear zonation from the diopsidic core to augitic rim. Abundant
577 Mag and melt inclusions were observed in the rim. (f) Amphibole associated with anorthite rich Pl
578 (An₉₅) occurring together with Cpx phenocryst in the gray pumice. (g) Mg# line-profile of the high-
579 Mg Ol. (h) Representative Cpx compositions in Ca-Mg-Fe ternary diagram.

580

581 Figure 5.

582 Back-scattered electron images of two-types of black enclave observed in the studied pumice. (a)
583 Type-1 black enclave exhibiting Cpx phenocrysts embedded in a dense groundmass composed of Pl,
584 Cpx, opaque minerals, and intergranular melt. (b) Type-2 black enclave exhibiting equigranular texture
585 of Cpx, Pl, and Ol, filled with intergranular melt. (c) Closed photo of (a) showing fine grains of Cpx,
586 Pl, and opaque minerals. (d) Zoned Pl occurred in type-2 black enclave, showing rim-ward decrease
587 in An content. A-B line indicates the position of the line profile shown in (e). (e) A-B line profile of
588 An content.

589

590 Figure 6

591 (a) Photomicrograph of the vesicular glass in gray pumice, almost free from microcrystals. (b)
592 Vesicular glass of black pumice exhibits brown color with fine sticky microcrystals of Cpx and rare
593 Ol. (c) Boundary of the black and gray pumice in BSE image. Gray pumice exhibits extensive
594 elongation. (d) Vesicular glass of amber pumice, exhibiting large size bubbles (>500 μm in diameter),
595 and almost colorless. (e) Vesicular glass of pale gray pumice. Abundant nanolites of sticky-shape and
596 small spot are observed (arrowed). (f) BSE image of the glass of pale gray pumice, showing abundant
597 nanolites in the glass. (g) Typical Raman spectra of the black nanolite in the pale gray pumice and
598 other glasses. The brown-colored glass of black pumice shows the magnetite peak at 663 cm^{-1} although
599 no crystal is visible under microscope observation.

600

601 Figure 7.

602 (a) Total alkali vs SiO₂ diagram of the vesiculated glass and whole-rock of the studied pumice clasts.
603 Also whole-rock analyses of previous studies are shown. (b) MgO-CaO binary diagram of the
604 vesiculated glass of the studied sample. Legends are similar to those of (a). (c) Spider diagram showing
605 trace element compositions of the whole-rock gray pumice (FOB-JMA-15, 18, and 19) determined by
606 solution ICP-MS, and vesiculated glass and selected mafic melt inclusions in FOB-JMA-18
607 determined by LA-ICP-MS. N-MORB data are sourced from Sun and McDonough (1989). (d)
608 Relationship between the time calculated from the diffusion modelling and applied f_{O_2} relative to QFM
609 buffer.

610

611 Figure 8.
612 Schematic picture of the FOB 2021 eruption from the preparing stage (A) to the explosive eruption
613 stage (C). Details are in text.
614

615 Tables

616 Table 1. Representative chemical composition of olivine and clinopyroxene.

617 Footnote

618 FeO*: total iron as FeO. Fe^{3+}/Fe^{2+} for clinopyroxene were calculated so that total cation =4 (O=6
619 basis). B.E.: Black enclave

620

621 Table 2. Representative chemical composition of plagioclase and opaque minerals.

622 Footnote

623 FeO*: total iron as FeO. Fe^{3+}/Fe^{2+} for opaque minerals were calculated so that sum of Fe^{2+} , Mn, and
624 Mg to be 1 (O=4 basis). Calculations of the Pl endmember were as follows: $An = Ca/(Ca+Na+K) \times 100$,
625 $Ab = Na/(Ca+Na+K) \times 100$, $Or = K/(Ca+Na+K) \times 100$. B.E.: Black enclave

626

627 Table 3. Representative chemical composition of volcanic glass determined by EMP analyses.

628 Footnote

629 FeO*: total iron as FeO. B.E.: Black enclave

630

631 Table 4. XRF whole-rock analyses of the selected pumice samples.

632

633 Table 5. Mass-normalized susceptibility of gray and black pumice samples.

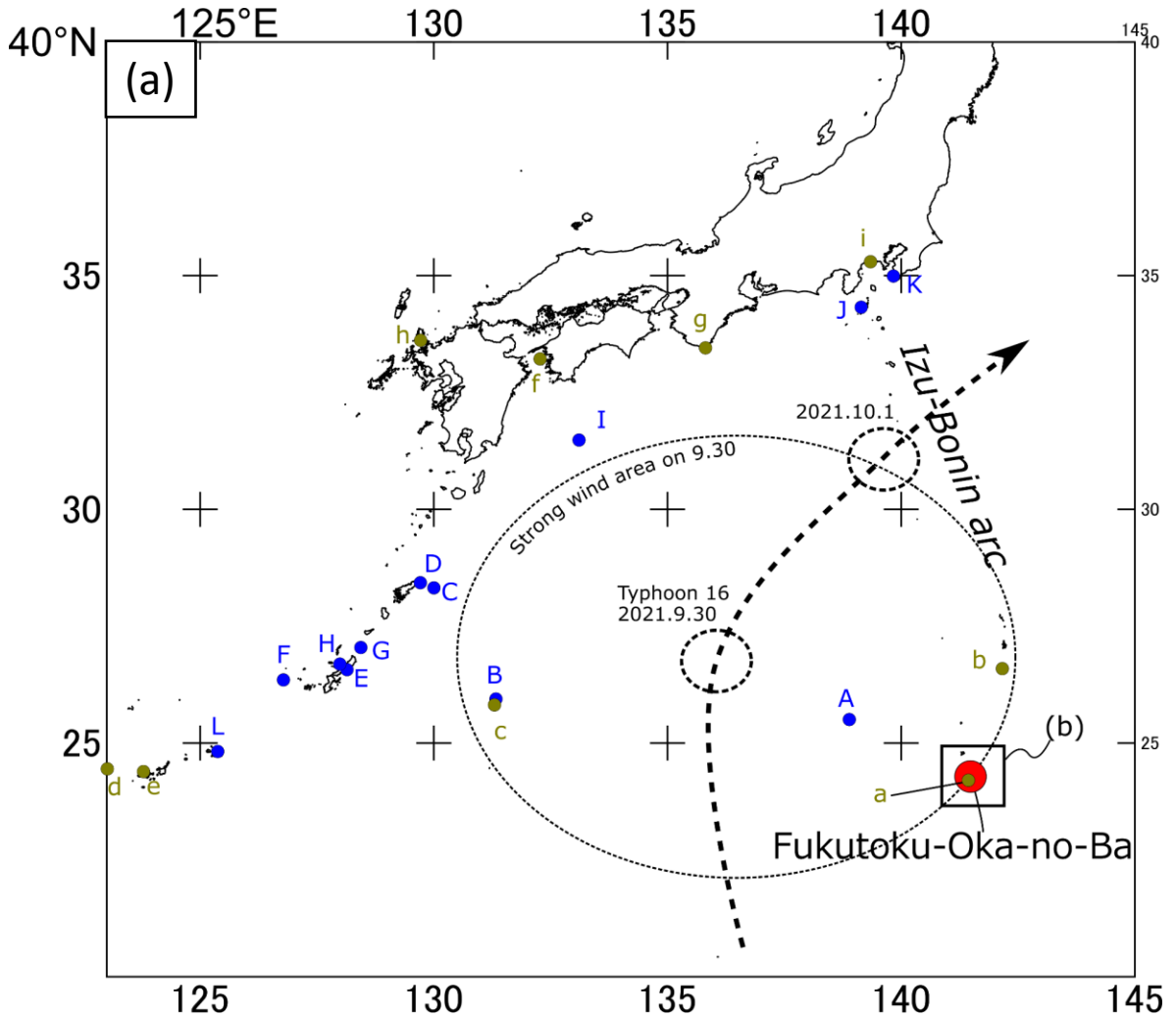
634

635 Table 6. Summary of the coexisting mineral and melt assemblages.

636

637 Table S1. Trace element analyses of glass of inclusions and groundmass, in addition to XRF whole-
638 rock analyses.

Figure 1



Timeline

2021 Aug. 13 eruption
 A: Aug 22 Sampling by RV *Keifu-Maru*
 B: Oct. 5 Twitter report from Kita-daito Isl.
 C: Oct. 10 Kikai Isl.
 D: Oct. 12 Amami-oshima Isl.
 E: Oct. 13 Okinawa Main Isl. East coast
 F: Oct. 13 Kume Isl.
 G: Oct. 14 Yoron Isl.
 H: Oct. 18 Okinawa Main Isl. West coast
 I: Oct. 30 Aircraft observation of the raft
 J: Nov. 10 Shikine Isl.
 K: Nov. 15 South Boso Peninsula
 L: Nov. 19 Miyako Isl.

1986 Jan. 18th eruption
 a. Jan. 20 Sampling by RV *Takuyo*
 b. Mar. 15 Hahajima Isl.
 c. Late May Minami-daito Isl.
 d. Late May Yonaguni Isl.
 e. < June 15 Iriomote Isl.
 f. June 26 Ehime Pref. Uwaumi
 g. Aug. Wakayama Pref. Kushimoto
 h. Oct. Genkai-nada
 i. 1991. Sept. Sagami Bay

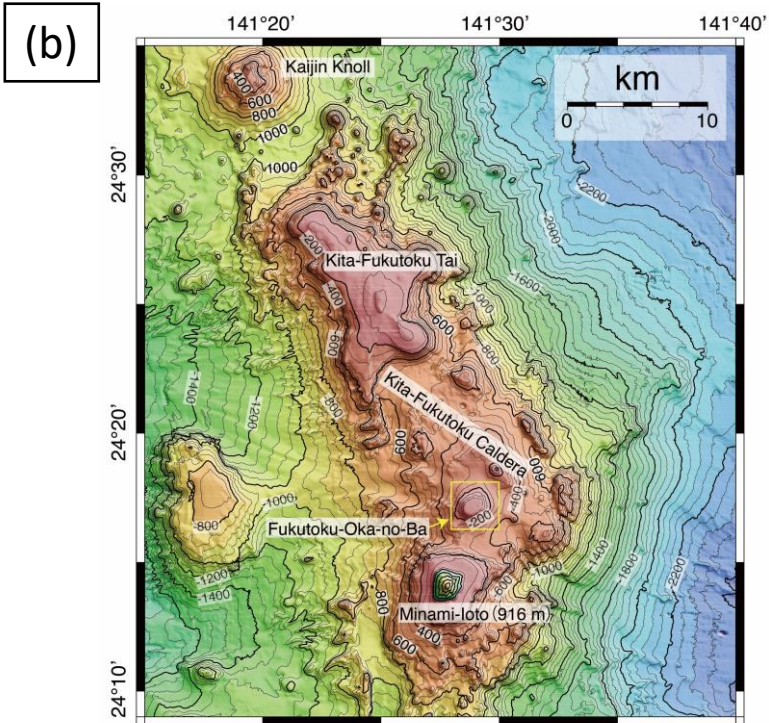


Figure 2

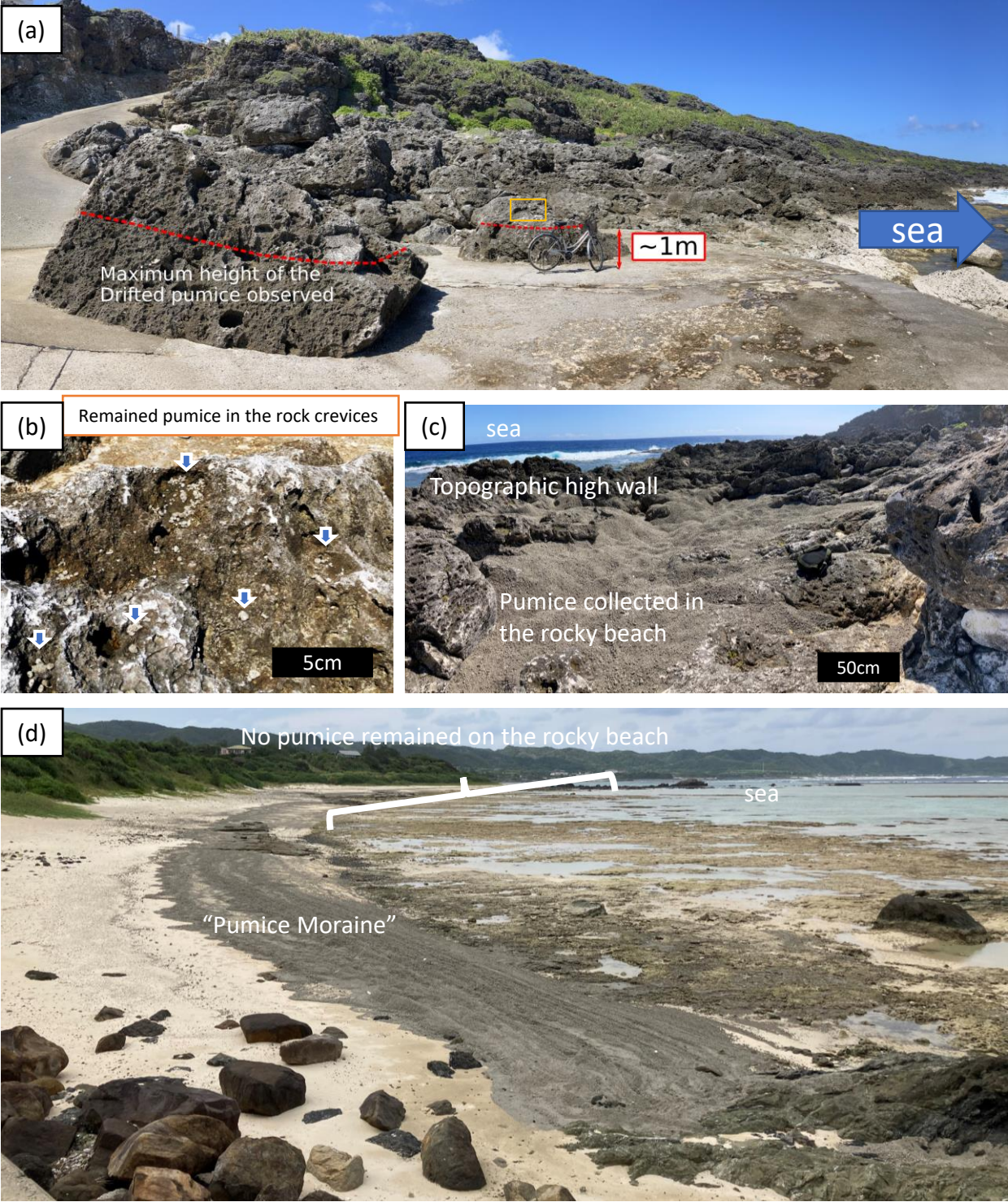


Figure 3

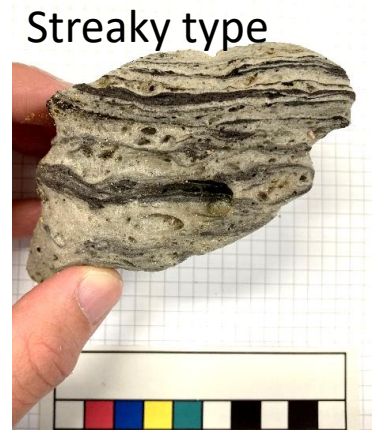
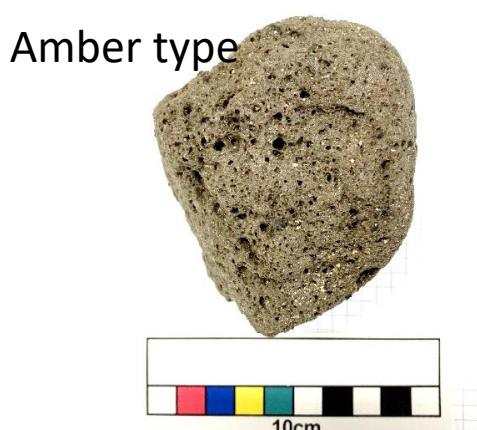
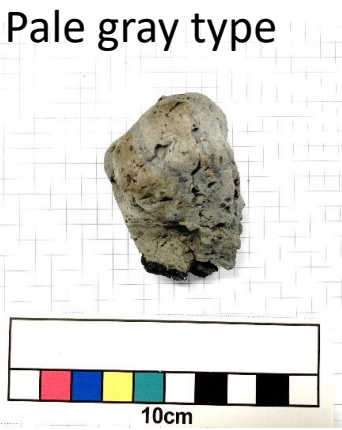
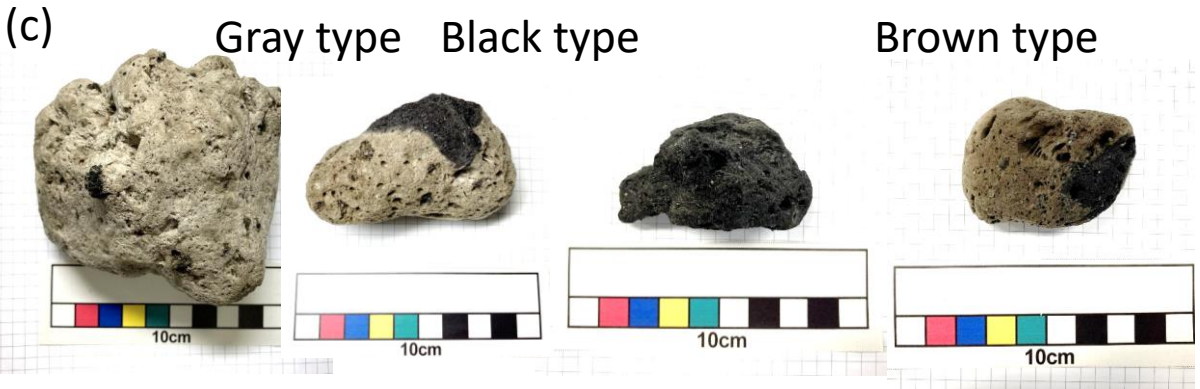
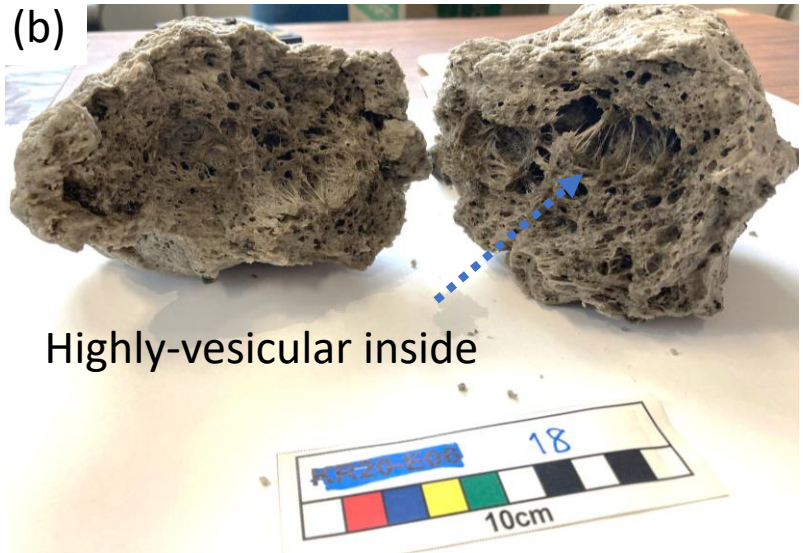


Figure 4

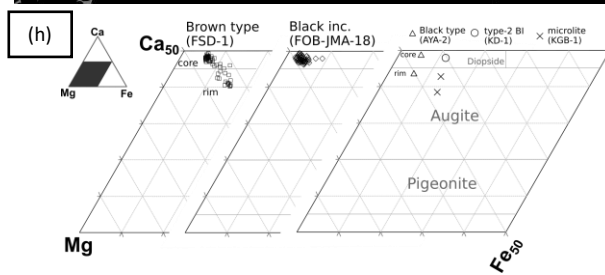
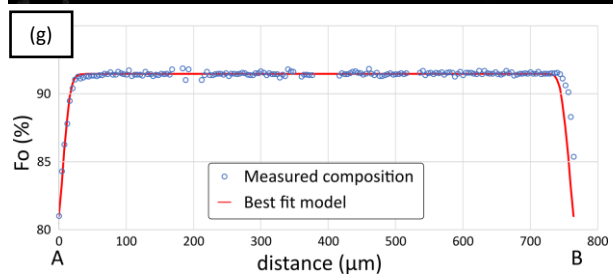
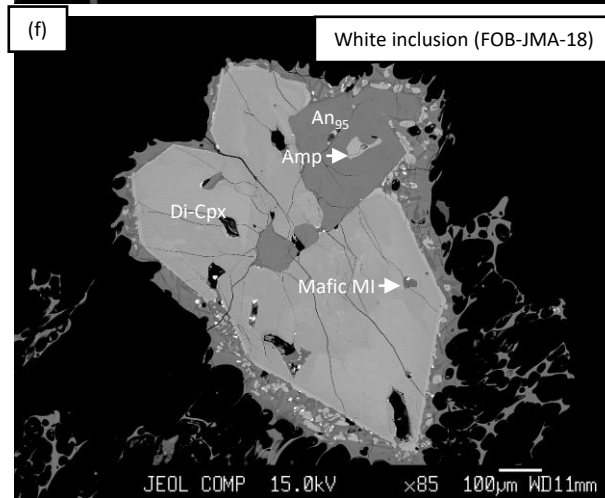
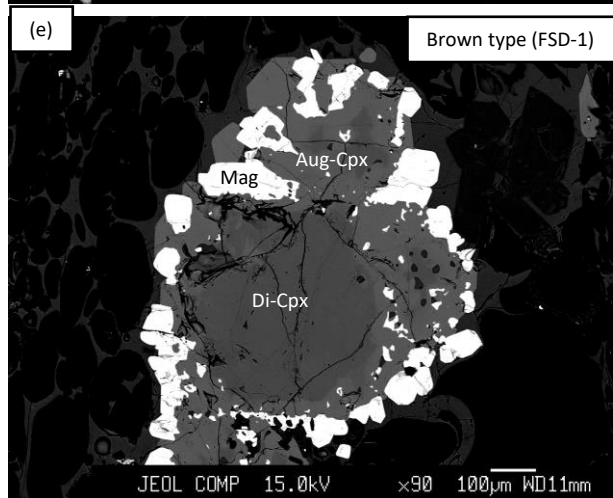
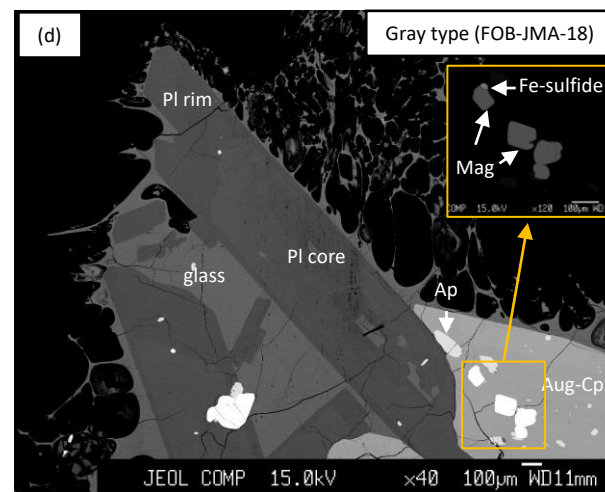
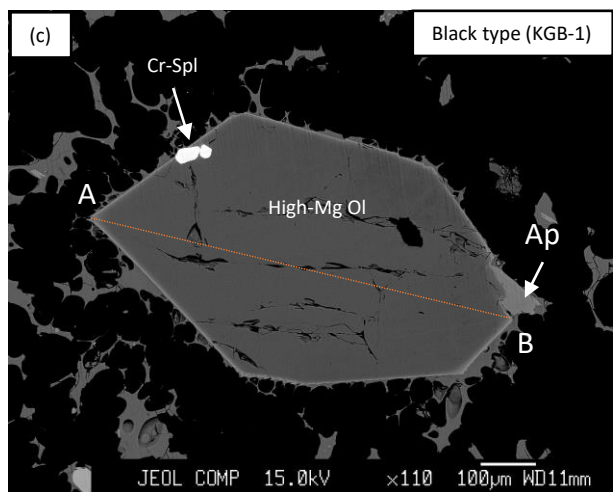
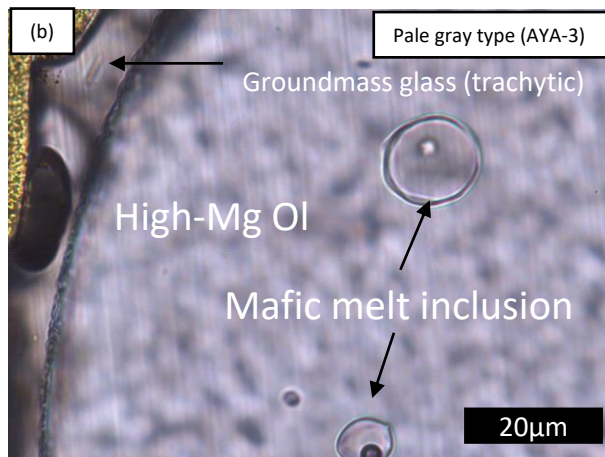
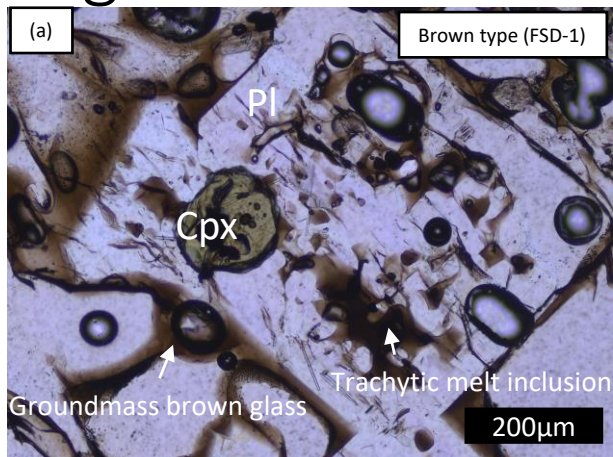


Figure 5

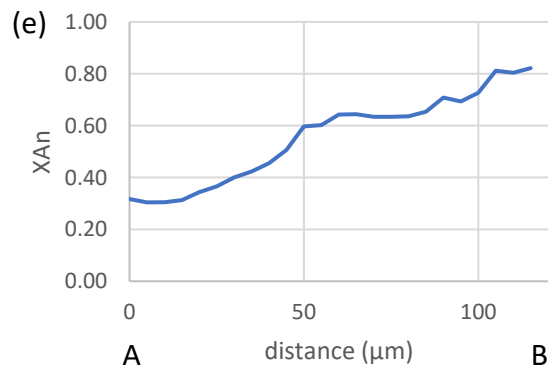
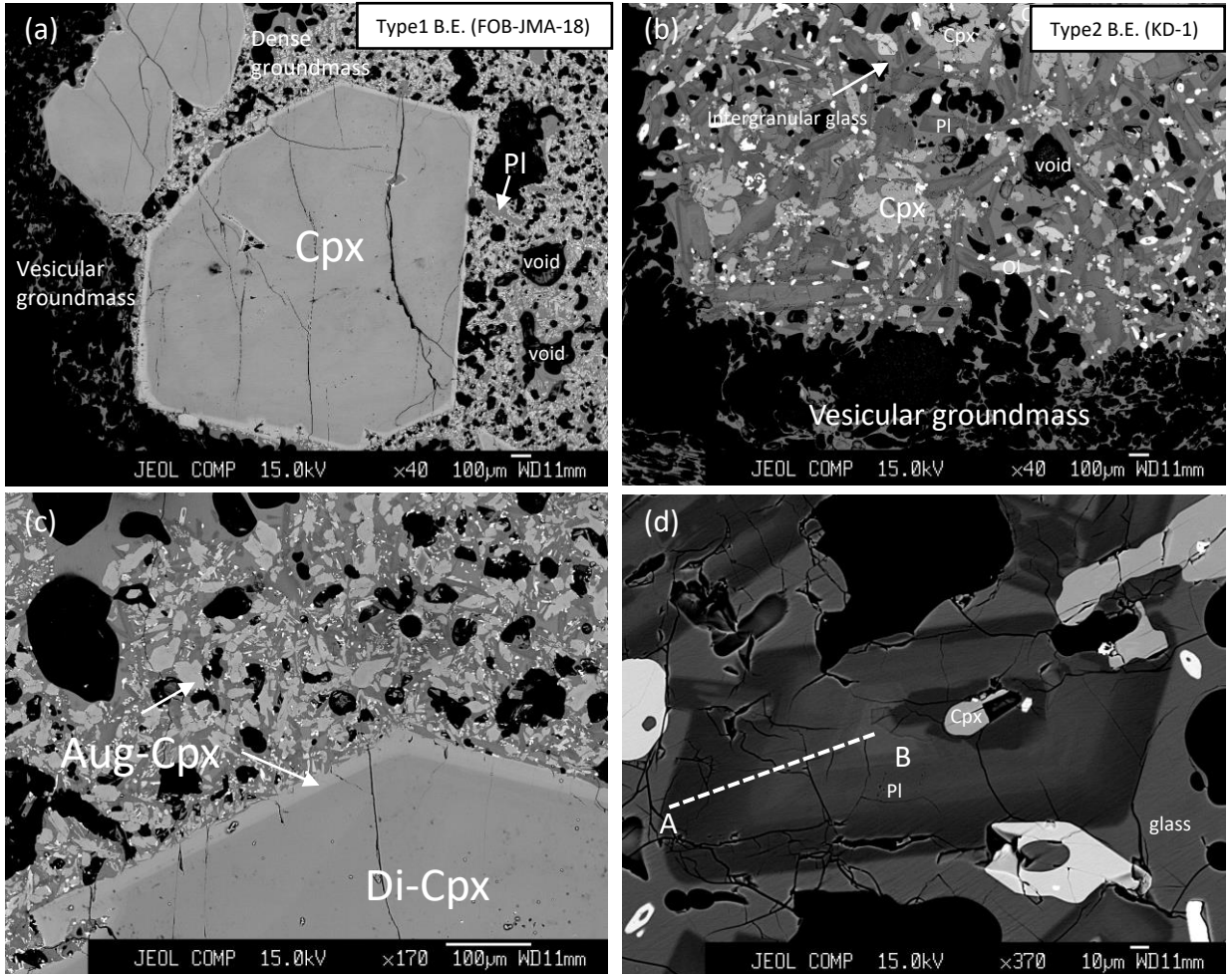


Figure 6

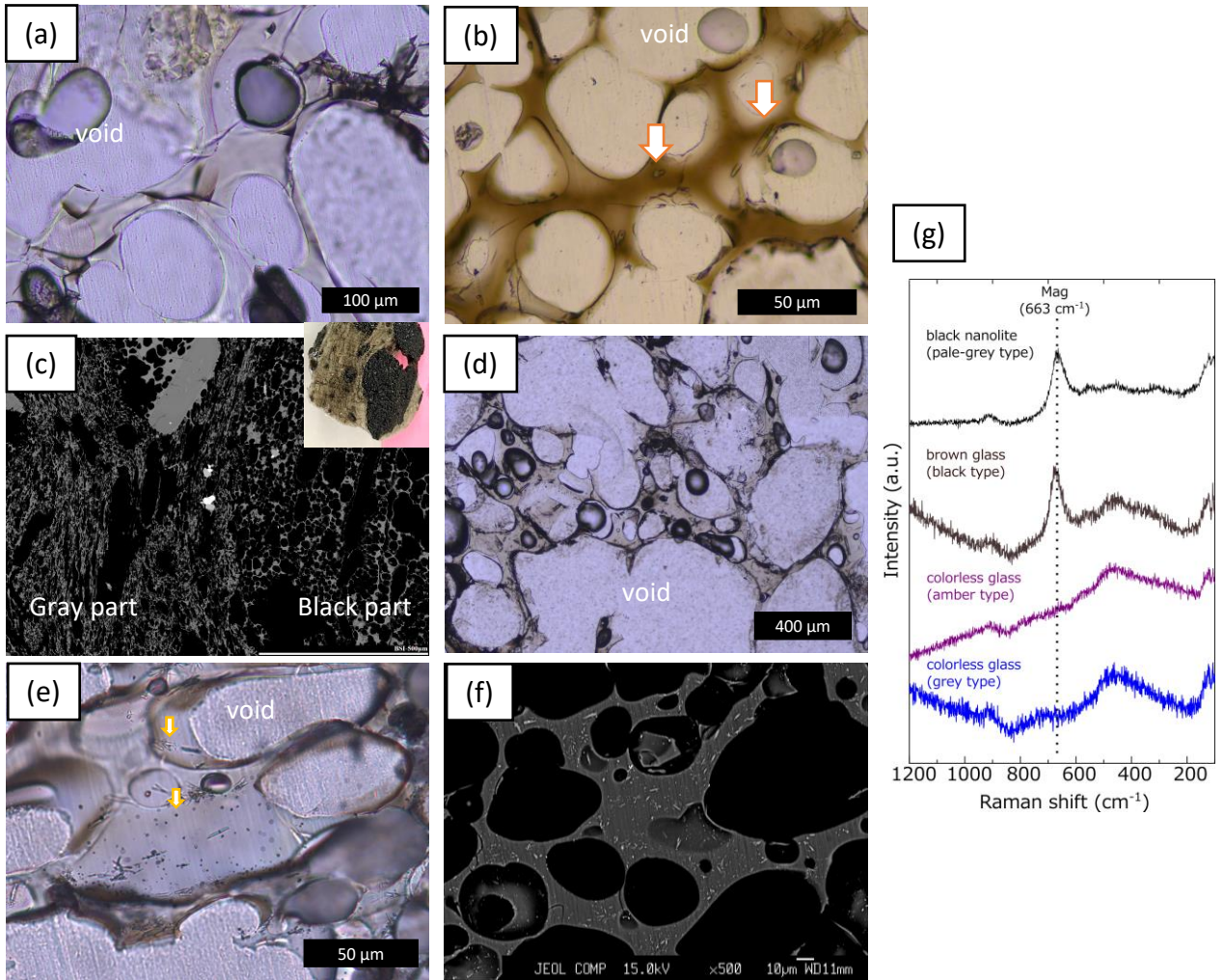


Figure 7

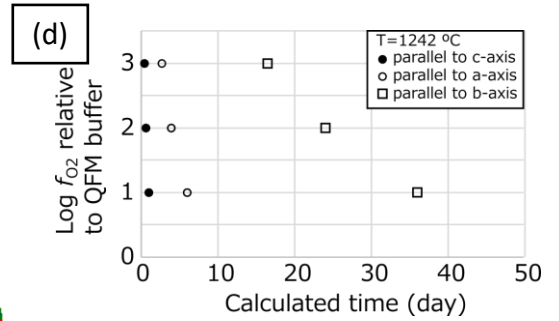
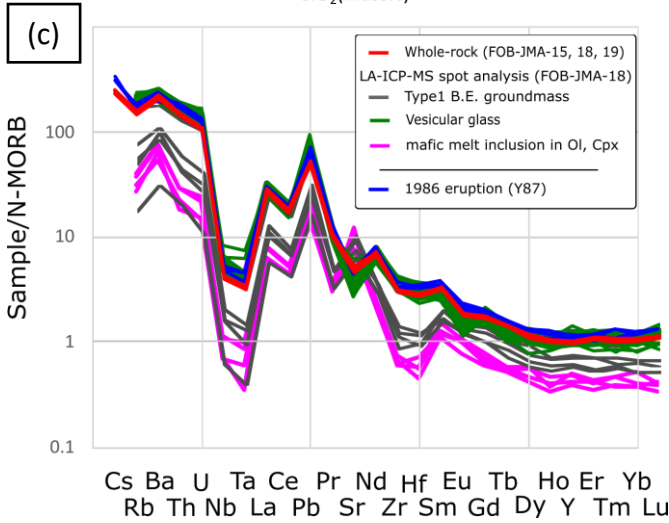
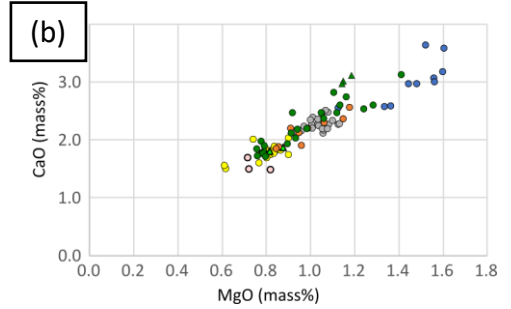
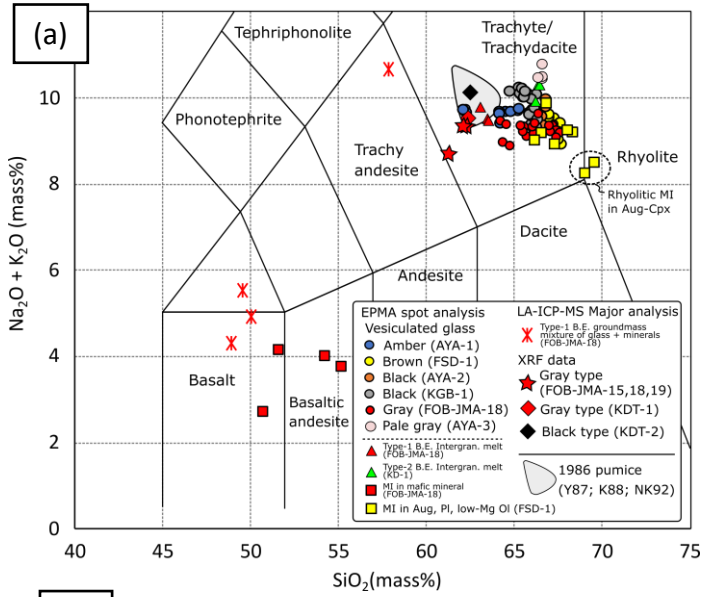


Figure 8

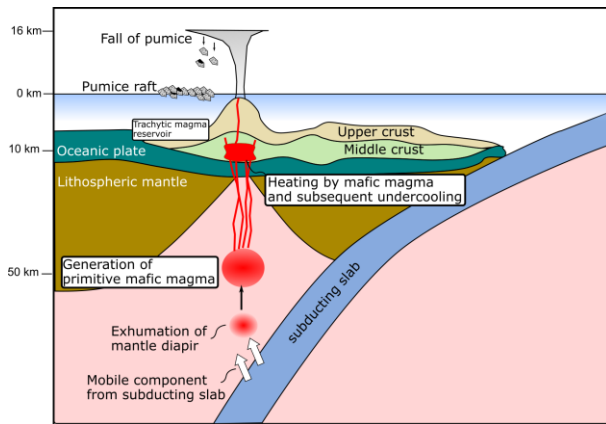


Table 1

Mineral	Ol						
	pumice type	Gray	Black		Brown	Type-1 B.E.	
site	Pacific ocean		Minami-daito		Amami	Pacific ocean	
sample No.	FOB-JMA-18		KGB-1		FSD-1	FOB-JMA-18	
note			core	rim	microlite		
SiO ₂		35.79	40.22	40.25	34.96	36.37	38.964
TiO ₂		0.01	0.00	0.01	0.00	0.00	0
Al ₂ O ₃		0.01	0.019	0.040	0.07	0.00	0.029
Cr ₂ O ₃		0.00	0.01	0.00	0.00	0.01	0.016
FeO*		30.31	8.18	17.47	29.23	29.66	14.226
MnO		1.56	0.15	0.47	1.26	1.52	0.254
MgO		32.39	50.42	41.79	33.79	32.61	46.032
CaO		0.14	0.34	0.18	0.20	0.15	0.336
Na ₂ O		0.00	0.01	0.00	0.00	0.00	0
K ₂ O		0.00	0.00	0.01	0.05	0.00	0
NiO		0.00	0.17	0.11	0.02	0.00	0.097
Total		100.21	99.53	100.32	99.58	100.32	99.95
O=		4	4	4	4	4	4
Si		0.98	0.99	1.02	0.96	0.99	0.98
Ti		0.00	0.00	0.00	0.00	0.00	0.00
Al		0.00	0.00	0.00	0.00	0.00	0.00
Cr		0.00	0.00	0.00	0.00	0.00	0.00
Fe ³⁺							
Fe ²⁺		0.69	0.17	0.37	0.67	0.67	0.30
Mn		0.04	0.00	0.01	0.03	0.03	0.01
Mg		1.32	1.84	1.58	1.38	1.32	1.72
Ca		0.00	0.01	0.00	0.01	0.00	0.01
Na		0	0.00	0.00	0.00	0.00	0.00
K		0	0.00	0.00	0.00	0.00	0.00
Ni		0.00	0.002	0.002	0.00	0.00	0.00
total cation		3.02	3.01	2.98	3.04	3.01	3.02
Mg#		0.66	0.92	0.81	0.67	0.67	0.67

Type-2 B.E. Kita-daito KD-1	Cpx						
	Grey		Black		Brown		host of rhyolitic MI
	Amami		Minami-daito		Amami		
	AYA-2		KGB-1		FSD-1		
	core	rim	core	microlite	core	rim	
36.737	50.49	49.30	52.12	50.52	51.45	52.61	53.43
0.035	0.30	0.72	0.27	0.75	0.27	0.39	0.32
0.012	5.10	5.67	3.38	4.26	3.89	1.48	1.13
0	0.00	0.00	0.39	0.02	0.12	0.01	0.00
30.282	6.32	8.92	4.57	8.76	4.28	9.35	9.91
1.498	0.10	0.19	0.00	0.45	0.11	0.83	0.86
32.21	14.62	13.30	15.56	14.52	16.06	15.35	15.26
0.17	23.21	21.34	23.15	19.63	23.76	19.71	19.50
0.011	0.22	0.33	0.10	0.41	0.07	0.45	0.40
0.012	0.02	0.01	0.02	0.03	0.02	0.05	0.00
0.005							
100.97	100.38	99.79	99.57	99.36	100.03	100.21	100.82
4	6	6	6	6	6	6	6
0.99	1.85	1.83	1.92	1.88	1.88	1.95	1.97
0.00	0.01	0.02	0.01	0.02	0.01	0.01	0.01
0.00	0.22	0.25	0.15	0.19	0.17	0.06	0.05
0.00	0.00	0.00	0.01	0.00	0.00	0.00	0.00
	0.08	0.06	0.00	0.04	0.07	0.06	0.02
0.68	0.11	0.21	0.14	0.24	0.07	0.23	0.29
0.03	0.00	0.01	0.00	0.01	0.00	0.03	0.03
1.29	0.80	0.74	0.85	0.81	0.87	0.85	0.84
0.00	0.91	0.85	0.91	0.78	0.93	0.78	0.77
0.00	0.02	0.02	0.01	0.03	0.01	0.03	0.03
0.00	0.00	0.00	0.00	0.00	0.00	0.00	0.00
0.00							
3.01	4.00	4.00	4.00	4.00	4.00	4.00	4.00
0.67	0.88	0.78	0.86	0.77	0.93	0.79	0.75

Type-1 B.E.	Type-2 B.E.	
Pacific ocean	Kita-daito	
FOB-JMA-18	KD-1	
core	rim	

53.60	49.23	49.53
0.20	0.43	0.76
1.63	4.94	5.49
0.24	0.07	0.08
3.21	8.46	9.45
0.06	0.07	0.42
17.54	14.63	13.04
24.24	22.06	21.55
0.12	0.16	0.39
0.02	0.01	0.00

100.87	100.05	100.71
--------	--------	--------

6	6	6
1.93	1.82	1.83
0.01	0.01	0.02
0.07	0.22	0.24
0.01	0.00	0.00
0.05	0.13	0.09
0.05	0.13	0.20
0.00	0.00	0.01
0.94	0.81	0.72
0.94	0.87	0.85
0.01	0.01	0.03
0.00	0.00	0.00

4.00	4.00	4.00
0.95	0.86	0.78

Table 2

pumice type site sample No. note	PI						
	Gray Pacific ocean FOB-JMA-18 core rim		Black Minami-dz KGB-1	Brown Amami FSD-1	Type-1 B.E. Pacific ocean FOB-JMA-18	Type-2 B.E. Kita-daito KD-1	core
SiO ₂	57.33	59.86	57.91	60.18	46.27	48.30	61.17
TiO ₂	0.05	0.00	0.05	0.00	0.05	0.03	0.03
Al ₂ O ₃	26.60	24.72	26.54	24.95	33.78	32.77	24.29
Cr ₂ O ₃	0.12	0.00	0.00	0.01	0.00	0.03	0.03
FeO*	0.56	0.46	0.55	0.58	1.05	0.81	0.56
MnO	0.06	0.00	0.12	0.00	0.01	0.05	0.00
MgO	0.02	0.05	0.04	0.04	0.14	0.03	0.03
CaO	9.00	7.30	9.06	7.09	17.35	16.24	6.17
Na ₂ O	5.81	6.54	5.78	6.57	1.39	1.89	6.50
K ₂ O	0.65	1.06	0.68	1.11	0.03	0.10	1.29
Total	100.18	99.98	100.73	100.52	100.07	100.24	100.06
O=	8	8	8.00	8.00	8.00	8.00	8.00
Si	2.57	2.68	2.59	2.68	2.13	2.21	2.72
Ti	0.00	0.00	0.00	0.00	0.00	0.00	0.00
Al	1.41	1.30	1.40	1.31	1.84	1.77	1.28
Cr	0.00	0.00	0.00	0.00	0.00	0.00	0.00
Fe ³⁺	0.00	0.00	0.00	0.00	0.00	0.00	0.00
Fe ²⁺	0.02	0.02	0.02	0.02	0.04	0.03	0.02
Mn	0.00	0.00	0.00	0.00	0.00	0.00	0.00
Mg	0.00	0.00	0.00	0.00	0.01	0.00	0.00
Ca	0.43	0.35	0.43	0.34	0.86	0.80	0.29
Na	0.51	0.57	0.50	0.57	0.12	0.17	0.56
K	0.04	0.06	0.04	0.06	0.00	0.01	0.07
total cation	4.99	4.98	4.98	4.98	5.01	4.99	4.95
An	44	36	45	35	87	82	32
Ab	52	58	51	59	13	17	60
Or	4	6	4	7	0	1	8

Opaque	Cr-Spl	Mag
	Black	Brown
	Minami-daito	Amami
	KGB-1	FSD-1
	in high-Mg Ol	in Cpx
	0.09	0.14
	0.25	10.46
	8.34	2.91
	58.20	0.11
	21.82	77.73
	0.31	0.87
	12.54	2.92
	0.02	0.00
	0.00	0.00
	0.00	0.00
	101.57	95.14
	4	4
	0.00	0.00
	0.01	0.28
	0.32	0.12
	1.48	0.00
	0.19	1.49
	0.39	0.82
	0.01	0.03
	0.60	0.15
	0.00	0.00
	0	0.00
	0	0.00
Cr#	0.74	
Mg#	0.60	0.15

Table 3

pumice type	Gray	Black	Amber	Pale gray	Brown			
site	Amami	Minami-daito	Amami	Amami	Amami			
sample No.	AYA2	KGB1	AYA1	AYA3	FSD-1			
note						MI in Cpx	MI in low- Mg Ol	MI in Pl
SiO ₂	65.63	65.22	64.69	65.56	67.67	65.89	66.75	
TiO ₂	0.52	0.49	0.46	0.53	0.55	0.50	0.37	
Al ₂ O ₃	16.10	16.12	16.05	15.89	16.05	16.15	15.78	
Cr ₂ O ₃	0.00	0.04	0.01	0.00	0.03	0.00	0.02	
FeO*	3.77	3.83	4.37	3.72	3.47	3.71	3.34	
MnO	0.05	0.09	0.33	0.18	0.02	0.14	0.17	
MgO	0.90	1.11	1.56	0.81	0.34	0.56	0.72	
CaO	2.15	2.24	3.07	1.46	0.95	1.94	1.57	
Na ₂ O	4.70	4.85	4.82	4.91	4.30	4.67	4.57	
K ₂ O	4.74	4.75	4.90	5.37	3.98	5.09	4.43	
P ₂ O ₅	0.11	0.14	0.17	0.19	0.07	0.18	0.07	
F	0.09	0.09	0.14	0.12	0.14	0.13	0.16	
Cl	0.31	0.30	0.29	0.36	0.35	0.39	0.33	
Total	98.65	98.86	100.43	98.61	97.42	99.33	97.77	

Type-1 B.E.		Type-2 B.E.	
Pacific ocean		Kita-daito	
FOB-JMA-18		KD-1	
MI in Cpx	MI in high- Mg Ol	intergranular	intergranular
51.92	48.93	62.63	65.53
0.53	0.57	0.33	0.41
20.91	16.39	16.12	16.29
0.08	0.00	0.00	0.00
5.59	9.04	5.83	3.95
0.25	0.18	0.22	0.21
3.43	3.96	1.13	0.87
9.17	14.87	2.97	1.85
2.91	1.78	4.54	4.74
0.91	0.82	4.84	5.05
n.a.	n.a.	0.51	0.20
0.04	0.02	0.21	0.11
0.14	0.09	0.44	0.32
95.68	96.54	99.11	99.11

Table 4

Pumice type	Gray	Gray	Gray	Gray	Black	Amber
site	Pacific ocean	Pacific ocean	Pacific ocean	Kita-daito	Kita-daito	Amami
Sample No.	FOB-JMA-15	FOB-JMA-18	FOB-JMA-19	KD-FOB1	KD-FOB2	AYA-01
SiO ₂	60.24	60.50	59.60	60.81	60.85	60.61
TiO ₂	0.58	0.58	0.56	0.57	0.61	0.57
Al ₂ O ₃	16.28	15.94	15.35	16.31	16.28	15.52
Fe ₂ O ₃	5.33	5.37	5.55	5.20	5.48	5.66
MnO	0.17	0.17	0.17	0.17	0.18	0.17
MgO	1.93	2.09	3.03	1.82	1.42	3.04
CaO	3.92	3.79	5.03	3.59	3.03	4.49
Na ₂ O	4.70	4.70	4.33	4.82	5.14	4.55
K ₂ O	4.34	4.42	4.10	4.43	4.65	4.27
P ₂ O ₅	0.23	0.23	0.21	0.23	0.28	0.22
Total	97.70	97.78	97.93	97.94	97.91	99.10
LOI	1.38	1.47	1.58	0.55	0.78	0.04

Table 5

	weight (g)	bulk mag. Sus. (cm ³)	MS (cm ³ /g)
Gray type	2.996	0.022	7.44E-03
Black type	4.857	0.045	9.23E-03

Table 6

	Mafic member	Trachytic member
Occurrence	Type-1 black inclusion xenocryst in black-/ pale gray- type	major member of pumice clasts
melt SiO ₂	48-55 mass%	62-70 mass%
OI Mg#	85-92	~65
Cpx composition	diopside	augite
Pl composition	An80-95	An33-44
Other minerals	amphibole	magnetite